





Improvement of superconducting properties in $\text{La}_{1-x}\text{Sr}_x\text{NiO}_2$ thin films by tuning topochemical reduction temperature

Motoki Osada ^{1,*}, Kohei Fujiwara ¹, Tsutomu Nojima ¹ and Atsushi Tsukazaki ^{1,2}

¹*Institute for Materials Research, Tohoku University, Sendai, Miyagi 980-8577, Japan*

²*Center for Science and Innovation in Spintronics, Core Research Cluster, Tohoku University, Sendai, Miyagi 980-8577, Japan*



(Received 4 March 2023; accepted 26 April 2023; published 18 May 2023)

The recently discovered nickelate superconductor with an infinite NiO_2 layer is synthesized via topochemical reduction with hydride reductant, which selectively removes apical oxygens from the perovskite precursor phase. While this thermodynamic process plays a crucial role in the materialization of the superconducting nickelate, optimizing the process is challenging due to the difficulty of controlling the selective disconnection and diffusion of oxygen in the perovskite phase. Here we demonstrate a significant improvement in the superconducting properties of $\text{La}_{1-x}\text{Sr}_x\text{NiO}_2$ by tuning the topochemical reduction temperature. By gradually increasing the reduction temperature, the $\text{La}_{1-x}\text{Sr}_x\text{NiO}_2$ films exhibit a transformation from the insulating state into the superconducting state, reaching a maximum onset of superconducting transition temperature T_c^{onset} of ~ 14 K at $x = 0.20$. Moreover, the normal state metallicity is drastically enhanced despite the slight variation in the crystal structure, implying that the electrical conduction in NiO_2 planes is likely a sensitive parameter to optimize the reduction state. The tunings of the reduced state in $\text{La}_{1-x}\text{Sr}_x\text{NiO}_{2+\delta}$ films with various Sr content x also corroborate that the optimal reduction temperature for inducing superconductivity increases with increasing x . The systematic optimization of reduction temperature results in an expansion of superconducting dome in temperature versus x phase diagram with higher T_c^{onset} and wider x region ($0.12 \leq x \leq 0.28$) compared to the previously reported diagram. Our findings provide a comprehensive understanding of the topochemical reduction process and its role in the electronic transport properties, leading to significant implications for the synthesis of low-valent nickelate superconductors.

DOI: [10.1103/PhysRevMaterials.7.L051801](https://doi.org/10.1103/PhysRevMaterials.7.L051801)

The square-planar structure, consisting of a four-coordinated transition metal oxide with a two-dimensional square lattice, offers a remarkable opportunity to investigate intriguing physical phenomena, for example superconductivity in cuprates $(\text{Nd}, \text{Ce})_2\text{CuO}_4$, coming from the specific ligand-field energy splitting [1,2]. This structure could be obtained by removing the apical oxygen from various precursor metal oxides through topochemical reduction, resulting in metastable phases with anomalous low-valent cation oxidation states, LaNiO_2 , NdNiO_2 , SrFeO_2 , and $\text{La}_4\text{Ni}_3\text{O}_8$ [3–8]. The recently discovered superconducting nickelate with infinite-layer structure $\text{Nd}_{0.8}\text{Sr}_{0.2}\text{NiO}_2$ has been synthesized by using this reduction technique [8]. The discovery of nickelate superconductors has ignited debates regarding the mechanism of superconductivity in a doped Mott insulator through similarities and differences with their cuprate counterparts. Both systems have a similar atomic structure based on the $3d^9$ electronic configuration. However, there is a distinct difference in the contribution of rare-earth $5d$ orbitals between these two. The Fermi surface of nickelates possesses a multiorbital nature, associated with partially occupied electron pockets primarily derived from the rare-earth $5d$ states and the two-dimensional hole band mainly originating from $\text{Ni } 3d_{x^2-y^2}$ states [9–13]. Furthermore, the weak hybridization

between $\text{Ni } 3d - \text{O } 2p$ resulting in the close Mott-Hubbard character makes nickelates unique [10,11].

Despite numerous theoretical investigations into this nickelate system [14–29], experimental demonstrations remain limited [30–38], and superconductivity in bulk samples is still absent [39–42]. One significant factor in these limited reports may be the difficulty of sample fabrication attributed to the chemical stability of the perovskite phase [43]. Another possible cause is the complexity of the topochemical reduction process, where selective removal of apical oxygens from a precursor phase leads to an anomalous low-valence cation oxidation state, namely Ni^+ [4,5]. Although several parameters, including the selection and amount of reduction agent and reduction time, are required to be optimized, the reduction temperature is an important parameter making a significant impact on the thermodynamic reaction. Figure 1(a) depicts a schematic diagram of the topochemical reduction of nickelates, where apical oxygens in NiO_6 octahedra of the precursor perovskite phase (LaNiO_3) are selectively removed, and it transforms into an infinite-layer structure with NiO_2 planes (LaNiO_2). When the reduction is insufficient, residual oxygen is believed to remain in the apical oxygen sites ($\text{LaNiO}_{2+\delta}$), which could potentially affect their physical properties. Given the similar atomic structure to their cuprate counterparts, the reduced valence of NiO_2 planes is considered as a key aspect to promote $3d^9$ electronic state in superconducting nickelates. With this notion, in this work, we explored the correspondence

*Corresponding author: mosada@tohoku.ac.jp

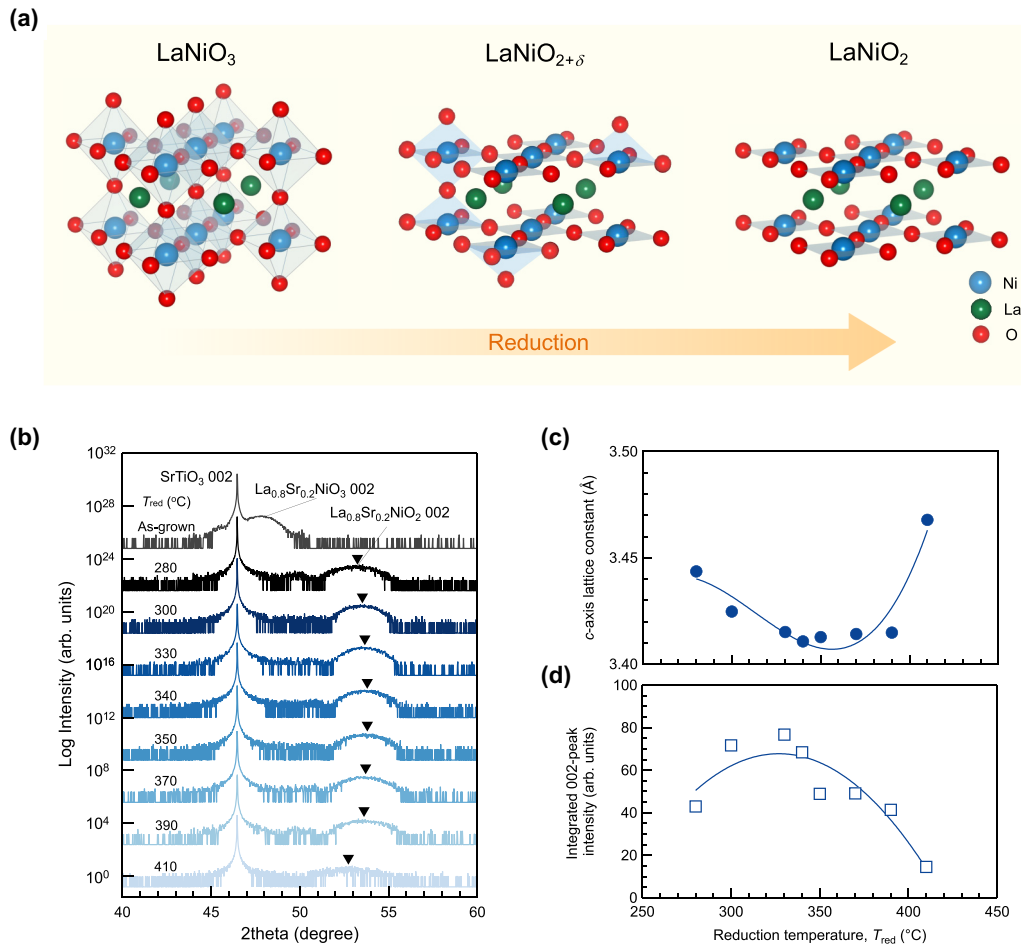


FIG. 1. (a) Conceptual schematic of the topochemical transformation from the perovskite phase LaNiO_3 (left) to the infinite-layer structure phase LaNiO_2 (right). The center schematic depicts the infinite-layer structure phase with residual oxygens as $\text{LaNiO}_{2+\delta}$. (b) X-ray diffraction θ - 2θ symmetric scans of perovskite nickelate $\text{La}_{0.8}\text{Sr}_{0.2}\text{NiO}_3$ and a series of reduced infinite-layer nickelate $\text{La}_{0.8}\text{Sr}_{0.2}\text{NiO}_2$ thin films. The filled triangle indicates the peak position used for the evaluation of c -axis lattice constant. (c) c -axis lattice constant of $\text{La}_{0.8}\text{Sr}_{0.2}\text{NiO}_2$ and (d) integrated 002-peak intensity of $\text{La}_{0.8}\text{Sr}_{0.2}\text{NiO}_2$ shown in (b) as a function of the reduction temperature. Solid curves represent guides to the eye.

between topochemical reduction temperature and electrical transport properties in $\text{La}_{1-x}\text{Sr}_x\text{NiO}_2$ thin films. The tuning of topochemical reduction temperature results in slight changes in structural parameters, but significantly improves both the normal state metallicity and superconductivity.

$\text{La}_{1-x}\text{Sr}_x\text{NiO}_3$ films were grown on SrTiO_3 (001) substrates using pulsed laser deposition, with $\text{La}_{1-x}\text{Sr}_x\text{Ni}_{1.2}\text{O}_y$ polycrystalline targets ablated by a KrF excimer laser (wavelength 248 nm). The SrTiO_3 (001) substrates were pre-annealed at 750°C in an oxygen partial pressure of 1×10^{-6} Torr to obtain an atomically flat surface. During growth, the substrate temperature was fixed at 520°C and the oxygen partial pressure was 200 mTorr. The laser fluence was 0.8 J/cm^2 and a repetition rate was 4 Hz. The film thickness was kept at a range 5–10 nm by adjusting the laser pulse counts, which were calibrated using x-ray reflectivity to determine the deposition rate. The film structure was analyzed using x-ray diffraction (XRD) techniques with $\text{Cu K}\alpha$ source. After deposition, samples were placed in a Pyrex glass tube with calcium hydride (CaH_2) powder ($\sim 0.1\text{ g}$), wrapped in aluminum foil to prevent direct contact with the powder. The glass tube

was sealed under vacuum (below 10 mTorr) using a methane gas torch and a rotary pump. We note that as a sufficient amount of CaH_2 is sealed in the glass tube compared to the molar amount of the films, tuning the reaction temperature can result in the adjustment of the amount of oxygen in the precursor perovskite phase. The sealed glass tube was then annealed in a tube furnace at various reduction temperatures (280 – 410°C) for 80 min, with ramping and cooling rates of 10°C/min . The first reduction was performed at 280°C for the $\text{Sr } x = 0.20$ sample (300°C for all other $\text{Sr } x$ samples). After XRD and transport measurements, the identical sample was again vacuum sealed in a glass tube with CaH_2 powder and annealed at a higher temperature of 300°C (320°C). This process was repeated with increasing reduction temperature until signs of decomposition were observed. The temperature T dependent resistivity ρ_{xx} was measured using a standard four-point geometry with Au wire bonded on In contact in a physical properties measurement system (PPMS, Quantum Design, Inc.). Note that $\rho_{xx}(T)$ for the $x = 0.28$ sample, which was reduced at 400°C , was measured down to $\sim 160\text{ mK}$, as a partial superconducting downturn was observed at 2 K.

Resistivity transition under the magnetic field along the crystal c -axis direction was measured up to 9 T.

For the $x = 0.20$ sample, we repeatedly reduced the identical piece of the sample at various reduction temperatures T_{red} (eight steps from 280 to 410° C). In Fig. 1(b), we show XRD θ - 2θ scans for the as-grown perovskite phase and a series of reduced infinite-layer structure phases, which consist of an infinitely repeated stacking sequence of NiO₂ square lattice plane and La/Sr plane. The peaks corresponding to (001)-oriented La_{0.8}Sr_{0.2}NiO₃ and La_{0.8}Sr_{0.2}NiO₂ are observed, respectively. By topochemical reduction, the perovskite phase transforms into the infinite-layer structure phase. As reducing the samples at higher T_{red} , 002 peaks (black solid triangles) shift to the higher angle side and eventually collapse at $T_{\text{red}} = 410^\circ\text{C}$. More quantitatively, we extracted the c -axis lattice constant using Gaussian fit in the 002 peak. As shown in Fig. 1(c), the c -axis lattice constant shrinks from 3.44 Å ($T_{\text{red}} = 280^\circ\text{C}$) to 3.41 Å ($T_{\text{red}} = 370^\circ\text{C}$), which is smaller than the previously reported value of 3.44 Å in La_{0.8}Sr_{0.2}NiO₂ thin films [33]. After the reduction at $T_{\text{red}} = 410^\circ\text{C}$, the 002 peak collapse and the corresponding c -axis lattice constant greatly increased to 3.47 Å, indicative of crystal decomposition due to over-reduction at high temperatures. In Fig. 1(d), we show the integrated 002-peak intensity, which was defined by integrating the XRD data over 2θ around the 002 peak. The integrated intensity reaches a maximum at $T_{\text{red}} = 330^\circ\text{C}$ and then systematically decreases with increasing T_{red} , suggesting improvement and degradation of the infinite-layer structure phase. The slight decrease of the c -axis lattice constant of approximately 1.0% likely reflects that the residual apical oxygens in the intermediate La_{0.8}Sr_{0.2}NiO_{2+ δ} state were removed uniformly, resulting in the adjustment of the Ni valence in the infinite-layer structure phase of La_{0.8}Sr_{0.2}NiO₂ with flat NiO₂ planes.

Given these minimal structural changes by topochemical reduction, which could enhance superconducting transition temperature T_c , we performed electrical transport measurements after each reduction process. Figures 2(a) and 2(b) exhibit temperature dependent resistivity $\rho_{xx}(T)$ for La_{0.8}Sr_{0.2}NiO₂ for $T_{\text{red}} = 280$ – 410°C . After the first reduction at $T_{\text{red}} = 280^\circ\text{C}$, the sample shows metallic behavior down to ~ 60 K and weakly insulating behavior at low temperatures. Overall, similar behavior is observed at $T_{\text{red}} = 300^\circ\text{C}$. Interestingly, the La_{0.8}Sr_{0.2}NiO₂ film after the reduction at $T_{\text{red}} = 330^\circ\text{C}$ exhibits superconducting transition. The corresponding onset temperature of superconductivity T_c^{onset} is ~ 8.1 K. Here, T_c^{onset} is defined as the intersection of two linear extrapolations from the normal state and the superconducting transition region. As shown in Fig. 2(b), the normalized resistivity with ρ_{xx} at $T = 20$ K shows up the variation of transition temperature. By further reduction at higher temperatures, it reaches the maximum T_c^{onset} of ~ 14 K at $T_{\text{red}} = 370^\circ\text{C}$ and then turns to a decrease in T_c^{onset} of ~ 11.5 K at $T_{\text{red}} = 410^\circ\text{C}$. This decrease in T_c is largely attributed to crystal decomposition due to excessively high reduction temperature, which is observed as the 002 peak diminishing in the XRD measurements [Fig. 1(b)] and increase of normal resistance [Fig. 2(a)].

One of the critical parameters evaluating the residual oxygens in NiO₂ planes is the residual resistivity ratio (RRR). To

determine RRR, $\rho_{xx}-T$ curves are normalized by the intercept resistivities at $T = 0$ K, which is defined by linear extrapolation of the normal state resistivity. Figure 2(c) demonstrates RRR curves in which a dashed line indicates a linear fit for the La_{0.8}Sr_{0.2}NiO₂ reduced at 370° C. As summarized in the inset of Fig. 2(c), RRR evolves with increasing T_{red} , reaches 10.4 at $T_{\text{red}} = 370^\circ\text{C}$, and then decreases after the reduction above $T_{\text{red}} = 390^\circ\text{C}$. These results suggest that normal metallicity is also improved by reduction temperature tuning. Furthermore, we observed that the temperature dependence of resistivity for reduced La_{0.8}Sr_{0.2}NiO₂ ($T_{\text{red}} = 350$ and 370°C) is approximately linear in temperature (T -linear) in the normal state, with exponents of approximately 1.02 and 0.94, respectively, in the temperature range 80–200 K. To discuss variations quantitatively, we extracted room-temperature resistivity ($T = 300$ K) $\rho_{300\text{K}}$ and T_c^{onset} as a function of T_{red} , as summarized in Figs. 2(d) and 2(e), respectively. $\rho_{300\text{K}}$ is minimized at intermediate $T_{\text{red}} = 340$ – 370°C and surges at high $T_{\text{red}} \geq 390^\circ\text{C}$; superconductivity emerges after reduction at 330° C and attains the highest T_c^{onset} of ~ 14 K at $T_{\text{red}} = 370^\circ\text{C}$. Moreover, we evaluated a correlation between the electrical transport properties and structural parameters, namely the c -axis lattice constant. Figures 2(f) and 2(g) show $\rho_{300\text{K}}$ and T_c^{onset} as a function of the c -axis lattice constant, respectively. We find that the short c -axis lattice constant seems preferable to the electrical properties with low ρ_{xx} and high T_c . In this study, superconductivity evolves with the c -axis lattice constant shorter than the value ~ 3.42 Å, which is found to be less than the previous report [33]. We note that even with the c -axis length of 3.47 Å ($T_{\text{red}} = 410^\circ\text{C}$), La_{0.8}Sr_{0.2}NiO₂ remains superconducting, potentially due to percolation of the residual superconducting region with partial crystal decomposition. Figures 2(h) and 2(i) show $\rho_{300\text{K}}$ and T_c^{onset} as a function of RRR, respectively. $\rho_{300\text{K}}$ tends to decrease and T_c^{onset} increases with increasing RRR, where the T_c value from the previous report also follows this trend [33], suggesting that metallicity above a certain threshold (RRR ~ 3 – 4) is necessary for the emergence of superconductivity.

These advances in materials quality by optimization of reduction temperature can be extended systematically to a broad range $x = 0.08$ – 0.32 . XRD results confirm the formation of a high-quality infinite-layer structure for all films with different x (see Fig. S1 of the Supplemental Material [44]); for each Sr doping ratio, developments of $\rho_{xx}-T$ curves by various T_{red} are shown in Fig. S2 of the Supplemental Material [44]. Figure 3(a) displays the $\rho_{xx}-T$ curves below 30 K for optimal reduced La_{1- x} Sr _{x} NiO₂ films ($0.08 \leq x \leq 0.32$). The inset of Fig. 3(a) shows $\rho_{xx}-T$ curves below 300 K. At low Sr doping ratio $x = 0.08$, the film shows metallic behavior down to ~ 40 K and an approximately logarithmic upturn at low temperatures, similar to those in other nickelate systems [33,36,37,45,46]. At high Sr doping ratio $x = 0.32$, metallic behavior with saturated residual resistance is analogous to overdoped cuprates. Importantly, superconductivity evolves at intermediate Sr doping ratio $x = 0.12, 0.16, 0.20, 0.24,$ and 0.28 , with $T_c^{\text{onset}} = 6.2, 13.9, 14, 8.4,$ and 1.6 K, respectively, exhibiting a substantial enhancement of T_c [33,34]. In the inset of Fig. 3(a), we also note that optimal Sr doped samples ($x = 0.16, 0.20,$ and 0.24) exhibit approximately T -linear resistivity in the normal state, while underdoped and over-

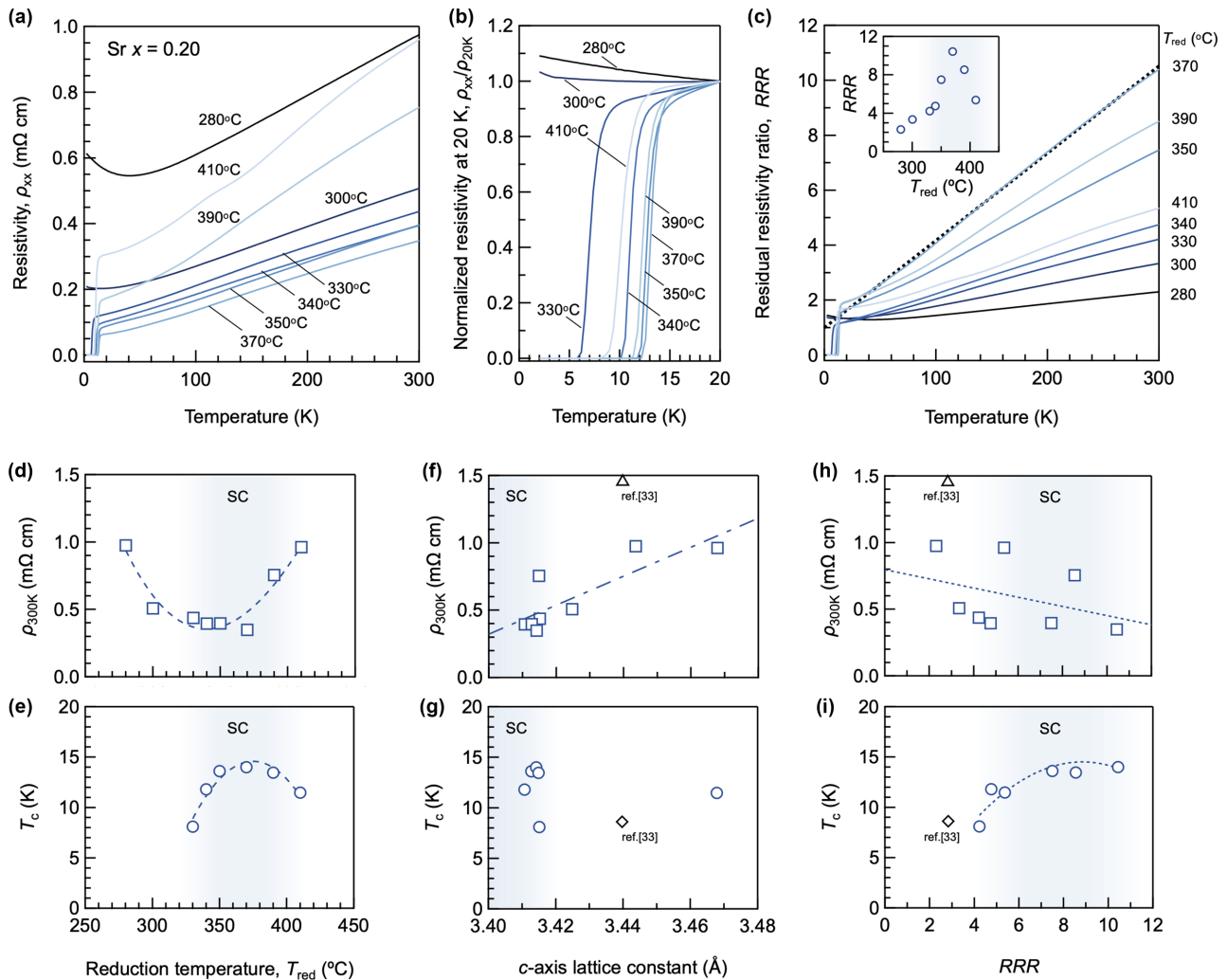


FIG. 2. (a) Temperature dependent resistivity $\rho_{xx}-T$ curves for $\text{La}_{0.8}\text{Sr}_{0.2}\text{NiO}_2$ thin films upon topochemical reduction. (b) The normalized resistivity with ρ_{xx} at $T = 20$ K. (c) The residual resistivity ratio, RRR, normalized by the intercept resistivities at 0 K, defined by linear fit of normal state resistivity. A dashed line indicates a linear fit for the sample reduced at 370°C . Inset shows RRR as a function of reduction temperature. (d) Resistivity at 300 K $\rho_{300\text{K}}$ and (e) the onset of superconducting transition temperature T_c^{onset} as a function of reduction temperature. (f) $\rho_{300\text{K}}$ and (g) T_c^{onset} as a function of c -axis lattice constant. (h) $\rho_{300\text{K}}$ and (i) T_c^{onset} as a function of RRR. Triangles and diamonds represent $\rho_{300\text{K}}$ and T_c^{onset} of previously reported values adapted from Ref. [33]. Dashed curves and lines represent guides to the eye.

doped regimes show non- T -linear resistivity, also observed in $\text{Nd}_{1-x}\text{Sr}_x\text{NiO}_2$ [45]. The correlation between the normal state metallicity and superconductivity is a hallmark of unconventional superconductivity [47–49]. For instance, in this type of superconductivity, the resistivity varies linearly with temperature within a narrow composition region around optimal doping levels, whereas it enters a non- T -linear metallic (Fermi liquid) state at the end of the superconducting dome (overdoped regime). Our results indicate that the interplay between the normal state metallicity and superconductivity might be a prominent nature of this nickelate system.

In Fig. 3(b), we present an electric phase diagram of $\text{La}_{1-x}\text{Sr}_x\text{NiO}_2$, where a superconducting dome appears from $x = 0.12$ to 0.28 with a maximum T_c^{onset} of 14 K at $x = 0.20$. The overall superconducting phase boundary is expanded to both the temperature and Sr doping directions compared to previous reports [30,31,33,34]. The maximum T_c in $\text{La}_{1-x}\text{Sr}_x\text{NiO}_2$ in this study is still lower than the recently

reported value in $\text{Nd}_{1-x}\text{Sr}_x\text{NiO}_2$ [45] and comparable to that of $\text{Pr}_{1-x}\text{Sr}_x\text{NiO}_2$ [46]. It is noteworthy that superconductivity is observed at even $x = 0.24$ and 0.28 with $T_c^{\text{onset}} = 8.4$ and 1.6 K, respectively. This result indicates the dramatic suppression of the disorder in the NiO_2 plane compared to the previous samples in spite of rich Sr doping. Both optimizations of crystalline quality of perovskite phase and reduction conditions are critically important to stabilize the superconducting NiO_2 planes. Based on these high quality films, further investigations can be addressed to the interesting phenomena in overdoped regions, such as Fermi-liquid transport behavior and stripe correlation, in nickelate systems. Furthermore, through systematic tuning of the reduction temperature for each Sr content, the optimum reduction temperature is determined, as shown in the inset of Fig. 3(b). Here, markers indicate the temperatures that result in the highest T_c for each Sr content; error bars signify temperature ranges where superconductivity emerges. Our results exhibit

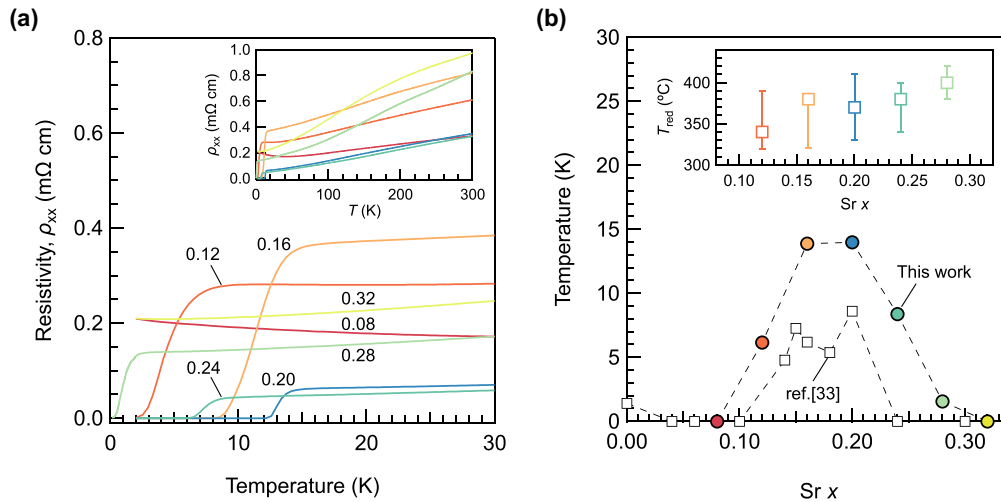


FIG. 3. (a) Representative temperature dependence of resistivity $\rho_{xx}-T$ curves below 30 K for optimally reduced $\text{La}_{1-x}\text{Sr}_x\text{NiO}_2$ thin films. The inset shows $\rho_{xx}-T$ up to 300 K. (b) The superconducting phase diagram of $\text{La}_{1-x}\text{Sr}_x\text{NiO}_2$ thin films, extracted from the $\rho_{xx}-T$ measurements. Circle represents T_c^{onset} of optimally reduced films in this study. Squares connected with a dashed line indicate previously reported values adapted from Ref. [33]. The inset shows the optimal reduction temperature as a function of Sr content. Squares indicate the temperature which induce highest T_c^{onset} for each Sr content. Error bars represent temperature range which induce superconductivity $\rho_{xx}-T$ data for Sr $x = 0.08, 0.12, 0.16, 0.24, 0.28,$ and 0.32 are shown in Fig. S2 of the Supplemental Material [44].

that the optimal reduction temperature for superconductivity rises as the Sr content increases. We attribute this tendency to the differences in the local energy potential surrounding the oxygens in various Sr doping ratios.

In order to obtain information about the coherence length, we measured the temperature dependence of resistivity for $\text{La}_{0.8}\text{Sr}_{0.2}\text{NiO}_2$ in magnetic fields $\mu_0 H$ along the c axis as shown in Fig. S3 of the Supplemental Material [44], where μ_0 is the vacuum permittivity. Figure 4(a) shows the

upper critical field $H_{c2,\perp}$ of samples reduced at various T_{red} . Here, $T_c(H)$ corresponding to the temperature on the $H_{c2,\perp}(T)$ line is defined as that for 50% resistivity at T_c^{onset} . For all $\text{La}_{0.8}\text{Sr}_{0.2}\text{NiO}_2$ samples, the suppression of a superconducting transition was observed by applying magnetic fields. As shown in Fig. 4(a), the $H_{c2,\perp}$ shows a T -linear dependence, which is represented by the following Ginzburg-Landau (GL) model:

$$\mu_0 H_{c2,\perp}(T) = \frac{\phi_0}{2\pi \xi_{ab}^2(0)} \left(1 - \frac{T}{T_c}\right), \quad (1)$$

where ϕ_0 is the quantum flux and $\xi_{ab}(0)$ is the in-plane zero-temperature coherence length. The extracted $\mu_0 H_{c2,\perp}(0)$ given by a linear extrapolation from $\mu_0 H_{c2,\perp}(T)$ curve are summarized in Fig. 3(b), which is on the line of previously reported values [50,51]. The corresponding $\xi_{ab}(0)$ obtained by the GL model were 41.2, 33.9, 32.3, 32.9, 34.5, and 36.5 Å for $T_{red} = 330, 340, 350, 370, 390,$ and 410°C , respectively, as shown in Fig. 3(c). This change in $\xi_{ab}(0)$ suggests that $T_{red} = 350-370^\circ\text{C}$ is an optimal T_{red} for $\text{La}_{0.8}\text{Sr}_{0.2}\text{NiO}_2$ with smaller $\xi_{ab}(0)$ than previously reported values (~ 42.6 Å for $\text{Nd}_{0.775}\text{Sr}_{0.225}\text{NiO}_2$ [52] and ~ 42.1 Å for $\text{La}_{0.8}\text{Sr}_{0.2}\text{NiO}_2$ [33]). These magnetotransport behaviors also guarantee the improvement of superconducting properties by tuning T_{red} .

In summary, we explored a reduction temperature tuning and its effect on both the normal and superconducting properties in the infinite-layer nickelate, namely, $\text{La}_{1-x}\text{Sr}_x\text{NiO}_2$. The change in reduction temperature causes only slight variations in crystal structures, but a dramatic improvement in electrical transport properties: a transformation from the insulating state to the superconducting state. We interpret that through optimal reduction, the residual apical oxygens are uniformly removed, leading to the superior electrical transport properties mainly at the NiO_2 plane. We reveal that optimal reduction temperature for superconductivity increases with increasing the Sr content,

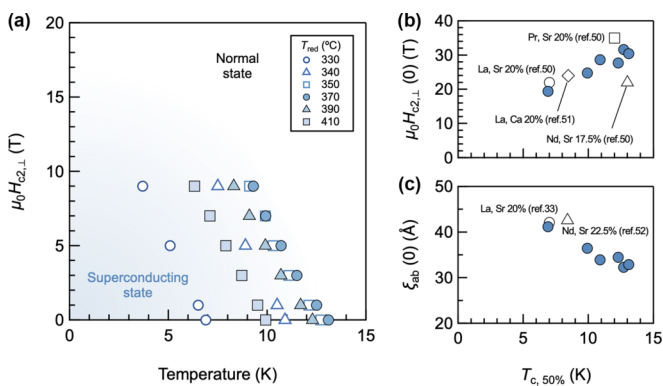


FIG. 4. (a) Upper critical field $\mu_0 H_{c2,\perp}$ vs midpoint T_c for $\text{La}_{0.8}\text{Sr}_{0.2}\text{NiO}_2$ thin films at different reduction temperature. $\rho-T$ curves under perpendicular magnetic field are shown in Fig. S3 of the Supplemental Material [44]. (b) Upper critical field at 0 K $\mu_0 H_{c2,\perp}(0)$ as a function of midpoint T_c . Open triangle, square, circle, and diamond show Sr 17.5% doped Nd nickelates, Sr 20% doped Pr nickelates, Sr 20% doped La nickelates, and Ca 20% doped La nickelates, respectively, adapted from Refs. [50,51]. (c) In-plane zero-temperature Ginzburg-Landau coherence length as a function of midpoint T_c . Open circle and triangle indicate Sr 20% doped La nickelates and Sr 22.5% doped Nd nickelates, respectively, adapted from Refs. [33,52].

implying the optimization of reduction temperature is critically important to obtain the superconductivity with various Sr contents. Furthermore, optimization of T_{red} for various doping levels expands the superconducting region in the phase diagram. Our observations imply the interplay between the reduced valence state of Ni and electrical conduction in NiO₂ planes tightly correlates each other. The T -linear metallicity in optimum samples indicates well-regulated NiO₂ planes with the suppression of disorder by appropriate reduction. Our findings will have significant implications for the synthe-

sis of low-valent nickelate superconductors in both thin film and bulk samples. Further investigation with newly optimized nickelates may lead to understanding of the superconducting phase and searching for as yet uncovered neighboring phases.

We thank K. Kisu and S. Orimo for technical support. This work was supported by JSPS KAKENHI (Grant No. 22K20347) and Grant Fund for Research and Education of Institute for Materials Research, Tohoku University.

The authors declare no competing interests.

-
- [1] Y. Tokura, H. Takagi, and S. Uchida, *Nature (London)* **337**, 345 (1989).
- [2] M. R. Norman, *Rep. Prog. Phys.* **79**, 074502 (2016).
- [3] M. Crespin, P. Levitz, and L. Gatineau, *J. Chem. Soc., Faraday Trans. 2* **79**, 1181 (1983).
- [4] M. A. Hayward, M. A. Green, M. J. Rosseinsky, and J. Sloan, *J. Am. Chem. Soc.* **121**, 8843 (1999).
- [5] M. A. Hayward and M. J. Rosseinsky, *Solid State Sci.* **5**, 839 (2003).
- [6] Y. Tsujimoto, C. Tassel, N. Hayashi, T. Watanabe, H. Kageyama, K. Yoshimura, M. Takano, M. Ceretti, C. Ritter, and W. Paulus, *Nature (London)* **450**, 1062 (2007).
- [7] J. Zhang, Y.-S. Chen, D. Phelan, H. Zheng, M. R. Norman, and J. F. Mitchell, *Proc. Natl. Acad. Sci. USA* **113**, 8945 (2016).
- [8] D. Li, K. Lee, B. Y. Wang, M. Osada, S. Crossley, H. R. Lee, Y. Cui, Y. Hikita, and H. Y. Hwang, *Nature (London)* **572**, 624 (2019).
- [9] K.-W. Lee and W. E. Pickett, *Phys. Rev. B* **70**, 165109 (2004).
- [10] B. H. Goodge, D. Li, K. Lee, M. Osada, B. Y. Wang, G. A. Sawatzky, H. Y. Hwang, and L. F. Kourkoutis, *Proc. Natl. Acad. Sci. USA* **118**, e2007683118 (2021).
- [11] M. Hepting, D. Li, C. J. Jia, H. Lu, E. Paris, Y. Tseng, X. Feng, M. Osada, E. Been, Y. Hikita, Y.-D. Chuang, Z. Hussain, K. J. Zhou, A. Nag, M. Garcia-Fernandez, M. Rossi, H. Y. Huang, D. J. Huang, Z. X. Shen, T. Schmitt *et al.*, *Nat. Mater.* **19**, 381 (2020).
- [12] M. Rossi, M. Osada, J. Choi, S. Agrestini, D. Jost, Y. Lee, H. Lu, B. Y. Wang, K. Lee, A. Nag, Y.-D. Chuang, C.-T. Kuo, S.-J. Lee, B. Moritz, T. P. Devereaux, Z.-X. Shen, J.-S. Lee, K.-J. Zhou, H. Y. Hwang, and W.-S. Lee, *Nat. Phys.* **18**, 869 (2022).
- [13] C. C. Tam, J. Choi, X. Ding, S. Agrestini, A. Nag, M. Wu, B. Huang, H. Luo, P. Gao, M. García-Fernández, L. Qiao, and K.-J. Zhou, *Nat. Mater.* **21**, 1116 (2022).
- [14] Y. Nomura, M. Hirayama, T. Tadano, Y. Yoshimoto, K. Nakamura, and R. Arita, *Phys. Rev. B* **100**, 205138 (2019).
- [15] P. Jiang, L. Si, Z. Liao, and Z. Zhong, *Phys. Rev. B* **100**, 201106(R) (2019).
- [16] P. Werner and S. Hoshino, *Phys. Rev. B* **101**, 041104(R) (2020).
- [17] A. S. Botana and M. R. Norman, *Phys. Rev. X* **10**, 011024 (2020).
- [18] M. Hirayama, T. Tadano, Y. Nomura, and R. Arita, *Phys. Rev. B* **101**, 075107 (2020).
- [19] X. Wu, D. Di Sante, T. Schwemmer, W. Hanke, H. Y. Hwang, S. Raghu, and R. Thomale, *Phys. Rev. B* **101**, 060504(R) (2020).
- [20] H. Sakakibara, H. Usui, K. Suzuki, T. Kotani, H. Aoki, and K. Kuroki, *Phys. Rev. Lett.* **125**, 077003 (2020).
- [21] S. Ryee, H. Yoon, T. J. Kim, M. Y. Jeong, and M. J. Han, *Phys. Rev. B* **101**, 064513 (2020).
- [22] F. Lechermann, *Phys. Rev. B* **101**, 081110(R) (2020).
- [23] J. Karp, A. S. Botana, M. R. Norman, H. Park, M. Zingl, and A. Millis, *Phys. Rev. X* **10**, 021061 (2020).
- [24] M. Kitatani, L. Si, O. Janson, R. Arita, Z. Zhong, and K. Held, *npj Quantum Mater.* **5**, 59 (2020).
- [25] M.-Y. Choi, K.-W. Lee, and W. E. Pickett, *Phys. Rev. B* **101**, 020503(R) (2020).
- [26] J. Kapeghian and A. S. Botana, *Phys. Rev. B* **102**, 205130 (2020).
- [27] E. Been, W.-S. Lee, H. Y. Hwang, Y. Cui, J. Zaanen, T. Devereaux, B. Moritz, and C. Jia, *Phys. Rev. X* **11**, 011050 (2021).
- [28] H. LaBollita and A. S. Botana, *Phys. Rev. B* **104**, 035148 (2021).
- [29] Y. Nomura and R. Arita, *Rep. Prog. Phys.* **85**, 052501 (2022).
- [30] D. Li, B. Y. Wang, K. Lee, S. P. Harvey, M. Osada, B. H. Goodge, L. F. Kourkoutis, and H. Y. Hwang, *Phys. Rev. Lett.* **125**, 027001 (2020).
- [31] S. Zeng, C. S. Tang, X. Yin, C. Li, M. Li, Z. Huang, J. Hu, W. Liu, G. J. Omar, H. Jani, Z. S. Lim, K. Han, D. Wan, P. Yang, S. J. Pennycook, A. T. S. Wee, and A. Ariando, *Phys. Rev. Lett.* **125**, 147003 (2020).
- [32] M. Osada, B. Y. Wang, B. H. Goodge, K. Lee, H. Yoon, K. Sakuma, D. Li, M. Miura, L. F. Kourkoutis, and H. Y. Hwang, *Nano Lett.* **20**, 5735 (2020).
- [33] M. Osada, B. Y. Wang, B. H. Goodge, S. P. Harvey, K. Lee, D. Li, L. F. Kourkoutis, and H. Y. Hwang, *Adv. Mater.* **33**, 2104083 (2021).
- [34] S. Zeng, C. Li, L. E. Chow, Y. Cao, Z. Zhang, C. S. Tang, X. Yin, Z. S. Lim, J. Hu, P. Yang, and A. Ariando, *Sci. Adv.* **8**, eab19927 (2022).
- [35] Q. Gu, Y. Li, S. Wan, H. Li, W. Guo, H. Yang, Q. Li, X. Zhu, X. Pan, Y. Nie, and H.-H. Wen, *Nat. Commun.* **11**, 6027 (2020).
- [36] X. Zhou, X. Zhang, J. Yi, P. Qin, Z. Feng, P. Jiang, Z. Zhong, H. Yan, X. Wang, H. Chen, H. Wu, X. Zhang, Z. Meng, X. Yu, M. B. H. Breese, J. Cao, J. Wang, C. Jiang, and Z. Liu, *Adv. Mater.* **34**, 2106117 (2021).
- [37] X. Ren, J. Li, W.-C. Chen, Q. Gao, J. J. Sanchez, J. Hales, H. Luo, F. Rodolakis, J. L. McChesney, T. Xiang, J. Hu, F.-C. Zhang, R. Comin, Y. Wang, X. J. Zhou, and Z. Zhu, *arXiv:2109.05761*.
- [38] G. A. Pan, D. F. Segedin, H. LaBollita, Q. Song, E. M. Nica, B. H. Goodge, A. T. Pierce, S. Doyle, S. Novakov, D. C. Carrizales, A. T. N'Diaye, P. Shafer, H. Paik, J. T. Heron, J. A.

- Mason, A. Yacoby, L. F. Kourkoutis, O. Erten, C. M. Brooks, A. S. Botana, and J. A. Mundy, *Nat. Mater.* **21**, 160 (2022).
- [39] Q. Li, C. He, J. Si, X. Zhu, Y. Zhang, and H.-H. Wen, *Commun. Mater.* **1**, 16 (2020).
- [40] B.-X. Wang, H. Zheng, E. Krivyakina, O. Chmaissem, P. P. Lopes, J. W. Lynn, L. C. Gallington, Y. Ren, S. Rosenkranz, J. F. Mitchell, and D. Phelan, *Phys. Rev. Mater.* **4**, 084409 (2020).
- [41] P. Puphal, Y. M. Wu, K. Fürsich, H. Lee, M. Pakdaman, J. A. N. Bruin, N. Jürgen, Y. E. Suyolcu, P. A. Van Aken, B. Keimer, M. Isobe, and M. Hepting, *Sci. Adv.* **7**, eabl8091 (2021).
- [42] P. Puphal, B. Wehinger, J. Nuss, K. Küster, U. Starke, G. Garbarino, B. Keimer, M. Isobe, and M. Hepting, *Phys. Rev. Mater.* **7**, 014804 (2023).
- [43] K. Lee, B. H. Goodge, D. Li, M. Osada, B. Y. Wang, Y. Cui, L. F. Kourkoutis, and H. Y. Hwang, *APL Mater.* **8**, 041107 (2020).
- [44] See Supplemental Material at <http://link.aps.org/supplemental/10.1103/PhysRevMaterials.7.L051801> for x-ray diffraction θ - 2θ symmetric scans of optimally reduced $\text{La}_{1-x}\text{Sr}_x\text{NiO}_2$ thin films and corresponding c -axis lattice constant; temperature dependent resistivity ρ_{xx} - T curves of $\text{La}_{1-x}\text{Sr}_x\text{NiO}_2$ thin films upon topochemical reduction for $x = 0.08, 0.12, 0.16, 0.24, 0.28, \text{ and } 0.32$; and resistivity of the $\text{La}_{0.8}\text{Sr}_{0.2}\text{NiO}_2$ thin film below 20 K at $\mu_0 H = 0, 1, 5, 9$ T for $T_{\text{red}} = 330$ and 340°C , and $\mu_0 H = 0, 1, 3, 5, 7, 9$ T for $T_{\text{red}} = 350, 370, 390, \text{ and } 410^\circ\text{C}$.
- [45] K. Lee, B. Y. Wang, M. Osada, B. H. Goodge, T. C. Wang, Y. Lee, S. P. Harvey, W. J. Kim, Y. Yu, C. Murthy, S. Raghu, L. F. Kourkoutis, and H. Y. Hwang, [arXiv:2203.02580](https://arxiv.org/abs/2203.02580).
- [46] M. Osada, B. Y. Wang, K. Lee, D. Li, and H. Y. Hwang, *Phys. Rev. Mater.* **4**, 121801(R) (2020).
- [47] S. Martin, A. T. Fiory, R. M. Fleming, L. F. Schneemeyer, and J. V. Waszczak, *Phys. Rev. B* **41**, 846(R) (1990).
- [48] L. Fang, H. Luo, P. Cheng, Z. Wang, Y. Jia, G. Mu, B. Shen, I. I. Mazin, L. Shan, C. Ren, and H.-H. Wen, *Phys. Rev. B* **80**, 140508(R) (2009).
- [49] J. Ayres, M. Berben, M. Čulo, Y.-T. Hsu, E. van Heumen, Y. Huang, J. Zaanen, T. Kondo, T. Takeuchi, J. R. Cooper, C. Putzke, S. Friedemann, A. Carrington, and N. E. Hussey, *Nature (London)* **595**, 661 (2021).
- [50] B. Y. Wang, T. C. Wang, Y.-T. Hsu, M. Osada, K. Lee, C. Jia, C. Duffy, D. Li, J. Fowlie, M. R. Beasley, T. P. Devereaux, I. R. Fisher, N. E. Hussey, and H. Y. Hwang, [arXiv:2205.15355](https://arxiv.org/abs/2205.15355).
- [51] L. E. Chow, K. Y. Yip, M. Pierre, S. W. Zeng, Z. T. Zhang, T. Heil, J. Deuschle, P. Nandi, S. K. Sudheesh, Z. S. Lim, Z. Y. Luo, M. Nardone, A. Zitouni, P. A. van Aken, M. Goiran, S. K. Goh, W. Escoffier, and A. Ariando, [arXiv:2204.12606](https://arxiv.org/abs/2204.12606).
- [52] B. Y. Wang, D. Li, B. H. Goodge, K. Lee, M. Osada, S. P. Harvey, L. F. Kourkoutis, M. R. Beasley, and H. Y. Hwang, *Nat. Phys.* **17**, 473 (2021).